Analyzing the footprints of near-surface aqueous turbulence: An image processing-based approach

J. Schnieders,[1] C. S. Garbe,[1] W. L. Peirson,[2] G. B. Smith,[3] and C. J. Zappa[4]

[1] In this contribution, a detailed investigation of surface thermal patterns on the water surface is presented, with wind speeds ranging from 1 to 7 m s^{-1} and various surface conditions. Distinct structures can be observed on the surface—small-scale short-lived structures termed fish scales and larger-scale cold streaks that are consistent with the footprints of Langmuir circulations. The structure of the surface heat pattern depends strongly on wind-induced stress. Consistent behavior regarding the spacing of cold streaks can be observed in a range of laboratory facilities when expressed as a function of water-sided friction velocity, u^*. This behavior systematically decreased until a point of saturation at $u^* = 0.7$ cm/s. We present a new image processing-based approach to the analysis of the spacing of cold streaks based on a machine learning approach to classify the thermal footprints of near-surface turbulence. Comparison is made with studies of Langmuir circulation and the following key points are found. Results suggest a saturation in the tangential stress, anticipating that similar behavior will be observed in the open ocean. A relation to Langmuir numbers shows that thermal footprints in infrared images are consistent with Langmuir circulations and depend strongly on wind wave conditions.

Citation: Schnieders, J., C. S. Garbe, W. L. Peirson, G. B. Smith, and C. J. Zappa (2013), Analyzing the footprints of near surface aqueous turbulence: An image processing-based approach, *J. Geophys. Res. Oceans*, *118*, 1272–1286, doi:10.1002/jgrc.20102.

1. Introduction

[2] Air-sea interaction is of fundamental environmental importance encompassing critical contemporary CO_2 uptake of the ocean and ocean warming. The key coupling processes dominate at scales far too small to be resolved in a large scale simulation of weather prediction or ocean currents. Thus, CO_2 fluxes show stronger variability on small scales than climatology can possibly predict [*Wanninkhof et al.*, 2011]. Gas exchange is closely linked to air-sea momentum exchange and the intensity of near-surface turbulence [*McKenna and McGillis*, 2004]. In this contribution, we present new detailed characterizations of the surface thermal signatures of near-surface turbulence and relate these to the surface forcing.

[3] Infrared imagery has been shown a useful tool to investigate surface layer processes and especially near surface turbulence [*Haußecker et al.*, 1995; *Jessup et al.* 1997; *Jähne and Haußecker*, 1998; *Schimpf et al.*, 1999; *Zappa et al.*, 2001; *Handler et al.*, 2001; *Haußecker et al.*, 2002]. *Garbe et al.* [2002, 2004] and *Schimpf et al.* [2004] have presented techniques based on passive thermography to estimate the heat flux and relate the scale of surface renewal events to wind speed and heat exchange. Thermographic techniques have also been used to investigate the features of near surface turbulence by *Melville et al.* [1998], *Handler et al.* [2001], *Veron and Melville* [2001], *Scott et al.* [2008], *Veron et al.* [2011], *Handler and Smith* [2011], and *Handler et al.* [2012].

[4] Here we use high-resolution infrared imagery to visualize the surface heat pattern that is formed by coherent turbulent structures immediately below the water surface. There are two key characteristics of observed surface heat patterns: (1) the surface heat patterns show characteristic features of scales and (2) the structure of these patterns changes with increasing wind stress and surface conditions.

[5] In the left image in Figure 1, a typical infrared image at moderate wind speeds is shown. A range of structural scales is visible. Clearly visible small-scale structures are superimposed by larger-scale temperature variations. These larger-scale structures are persistent as shown in the right image of Figure 1. The infrared image on the left is a representative sample from a sequence of 1000 infrared images. The right panel in Figure 1 shows the temporal development at a set line in the image stack highlighting the larger-scale cold surface streaks that persist throughout the sequence for approximately 16 s.

[1]Interdisciplinary Center for Scientific Computing (IWR), University of Heidelberg, Heidelberg, Germany.
[2]Water Research Laboratory, University of New South Wales, Sydney, Australia.
[3]Naval Research Laboratory, Washington, DC, USA.
[4]Lamont-Doherty Earth Observatory, Columbia University, Palisades, New York, USA.

Corresponding author: C. S. Garbe, Interdisciplinary Center for Scientific Computing (IWR), University of Heidelberg, Speyerer Str. 6, 69115 Heidelberg, Germany. (Christoph.Garbe@iwr.uni-heidelberg.de)
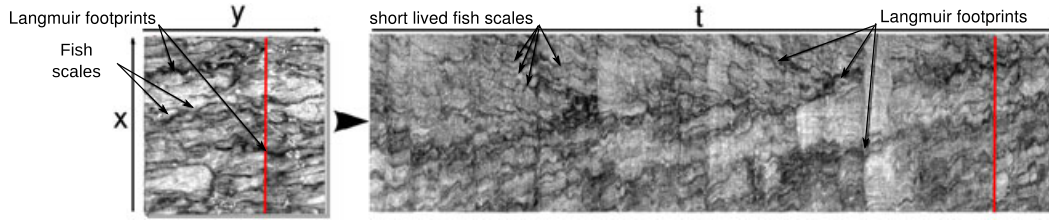
Figure 1. A stack of infrared images on the left side, taken in the Aeolotron, Heidelberg, at a friction velocity of $u^* = 0.34$ cm/s, is transformed into the right representation in which the temporal development of structures at a set position is described.
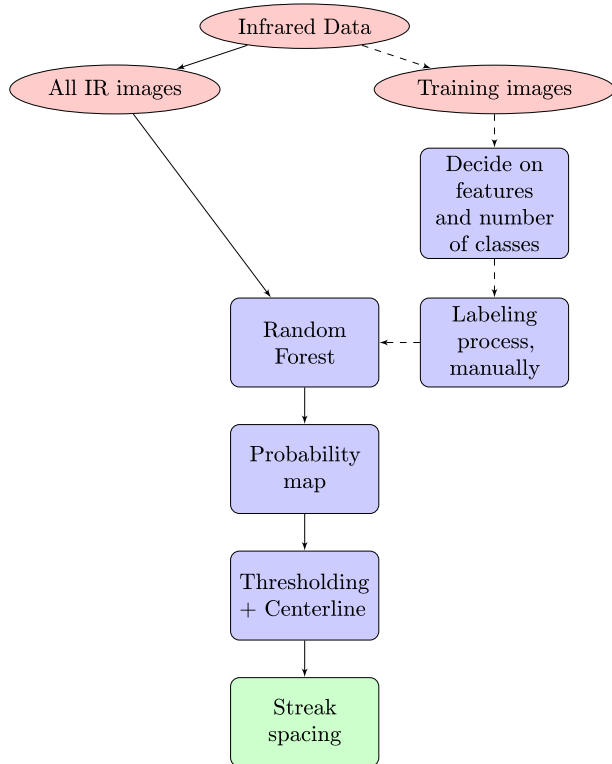

Figure 2. Classification algorithm. The original data set is split into two subsets: statistically independent images for the labeling process and all remaining images. Once a random forest is created, all remaining images can be analyzed.

[6] The typical small-scale heat pattern at the water surface consists of narrow cool bands and resembles fish scales [*Handler et al.*, 2001]. In the left panel of Figure 1, the resemblance of the thermal footprints to fish scale structures can easily be recognized; in the right time-based panel in Figure 1, they appear as little short-lived structures throughout the sequence. It has been observed and described in infrared imagery by *Handler et al.* [2001], *Scott et al.* [2008], *Handler and Smith* [2011], and *Handler et al.* [2012] and numerical simulations by *Handler et al.* [2001] and *Tsai et al.* [2005], but its exact nature has so far not been shown, although a good deal is known about the universally observed fish scales.

[7] Numerical simulations conducted by *Tsai et al.* [2005] and experiments by *Rashidi and Banerjee* [1990] have shown that wind stress alone without surface waves leads to the appearance of coherent turbulent structures.

[8] The streaky pattern observed at the water surface is very similar to the pattern of low-speed streaks near no-slip walls as described by *Nakagawa and Nezu* [1981] and *Smith and Metzler* [1983], and it has been suggested [*Tsai et al.*, 2005] that low-speed streaks near a no-slip wall and high-speed streaks near the water surface originate from the same mechanism. Their spacing was found to be log-normally distributed with a mean dimensionless streak spacing of $l^+ = lu^*/\nu = 100$, where the mean streak spacing is given by l, the (water-sided) friction velocity by u^*, and the kinematic viscosity by ν. The factor u^*/ν, by which l is non-dimensionalized, is estimated to correspond to the thickness of the thermal boundary layer [*Grassl*, 1976].

[9] The generally agreed scaling of $l^+ = lu^*/\nu = 100$ leads to the scaling of the streak spacing with the friction velocity u^*. Therefore, if the forcing mechanism is the same as that forcing the water surface, spacing of the streaks is supposed to decrease with increasing u^* in the regime of low wind speeds [*Scott et al.*, 2008].

[10] The strong correlation of the size of the fish scales with increasing wind stress can be seen in Figure 5. For comparison, the theoretically expected value of l is represented by the blue bar in the left corner of each panel, assuming $l^+ = 100$ as in the case of a no-slip wall, the average spacing that was determined here is shown in red (see section 4).

[11] Another possible production process is that of convective cells elongated by shear stress. [*Soloviev and Schlüssel*, 1994] suggested a critical surface Richardson number $Rf_{cr} = -\alpha g\nu/u^{*4} = -1.510^{-4}$ with the thermal expansion coefficient α, the kinematic viscosity ν, the friction velocity u^*, and $q_0 = -Q_0/c_p\rho$ with the vertical total heat flux q_0, the specific heat c_p, and the density ρ of water to describe the transition between free and forced convection.

[12] The conclusion might be that these streaks are caused by shear-induced turbulence, but still the question for the formation mechanism remains. *Tsai et al.* [2005] point out that one possible mechanism is that of horse shoe vortices that form in the turbulent shear layer by turning and stretching the spanwise vortices. These coherent turbulent structures move upward until their upper ends burst into the surface and therefore cause the upwelling of warmer and slower water at the surface. *Chernyshenko and Baig* [2005] suggest another mechanism for the formation of streaks. In this scheme, the lift-up of the mean profile in combination with shear stress and viscous diffusion together lead to the formation of the streaky pattern.

[13] Different methods for analyzing the small-scale surface heat pattern have been used, for example, Fourier analysis by *Handler et al.* [2001, 2012], manually counting (on numerical data) by *Tsai et al.* [2005], wavelet analysis by *Scott et al.* [2008], and a statistical analysis by *Handler and Smith* [2011]. The downside of these methods is that it is either very time consuming and not practicable for large numbers of conditions and images, or there is no or poor spatial determination of the streaks plus an overlying effect of small- and larger-scale streaks.

[14] To overcome the problems associated with spectral analysis and visual inspection, we chose an image processing-based approach to identify the thermal footprints of near-surface turbulence. This way, an overlying effect of small and large scales is avoided and the streak spacing can accurately be determined. Small-scale short-lived and large-scale long-lived structures (see Figure 1) are thus distinguished in this study.

[15] The larger-scale cold streaks in the infrared images are consistent in scale and spacing with the Langmuir circulation-induced cold surface streaks observed in infrared images and other visualization techniques by *Gemmrich and Hasse* [1992], *Caulliez* [1998], *Melville et al.* [1998], and *Veron and Melville* [2001] and also only appear in the presence of surface waves.

[16] They can bee seen in the infrared image in the left panel in Figure 1 but more clearly in the right time-based panel as they are not only clearly larger but also more persistent than the little short-lived fish scale structures.

[17] Langmuir circulations (LCs) were first discovered on very large scales on the ocean. Foam and seaweed form streaks with a spacing of one to several hundred meters and stretch across the waves in the direction of the wind for often several kilometers. The process that causes the streaky pattern at the water surface was first observed by Langmuir (1938). He concluded that there were zones of downwelling below the visible lines of foam and seaweed. These zones of downwelling are connected to zones of upwelling, causing zones of surface convergence and divergence. These structures can extend up to several kilometers in wind direction.

[18] Langmuir circulations of very different spacings and persistence have so far been observed, but generally there seem to exist more unstable Langmuir circulations of smaller scales that occur between more stable ones with larger scales [*Leibovich*, 1983]).

[19] *Craik and Leibovich* [1976] developed the Craik-Leibovich set of equations (CL II) to describe the underlying process:

$$\frac{\partial u}{\partial t} + v\frac{\partial u}{\partial t} + w\frac{\partial u}{\partial t} = La\ \nabla^2\ u \tag{1}$$

$$\frac{\partial \Omega}{\partial t} + v\frac{\partial \Omega}{\partial t} + w\frac{\partial \Omega}{\partial t} = La\ \nabla^2\ \Omega - \frac{du_s}{dz}\frac{\partial u}{\partial y} \tag{2}$$

with velocities u, v, and w, the Langmuir number La, the vorticity Ω, and the Stokes drift given by $u_s = 2S_0\ e^{2\beta z}$, S_0, and β empirical constants.

[20] The flow is governed by the dimensionless Langmuir number [*Leibovich and Paolucci*, 1981] representing the quotient of viscous forces, e.g., the diffusion of downwind viscosity and inertial forces which produce the vorticity by vortex tilting and stretching by the effect of waves [*Thorpe*,

2004]. In the case of monochromatic waves with a fixed frequency f, wave number k, and amplitude a, the Langmuir number can be defined as [*Leibovich and Paolucci*, 1981]

$$La = \left(\frac{v_t^3 k^2}{fa^2 u^{*2}}\right)^{1/2} \tag{3}$$

These equations show the coupling of two main features of transport of momentum across the air-sea interface: Langmuir circulations (LCs) develop because of the interaction of surface stress (friction velocity u^*) and surface waves (Stokes drift u_s).

[21] These equations cannot be solved analytically. Nevertheless under certain assumptions (if the Stokes drift is constant in time and linearly decaying with depth) and estimates (velocity perturbations of the order $\sqrt{La}$ and downwelling velocity of order La) derived from a numerical simulation, some features of idealized Langmuir circulations can be shown analytically [*Chini*, 2008].

[22] More recently, in laboratory measurements as well as in field experiments, a kind of small-scale Langmuir circulation has been observed and examined [for example by *Gemmrich and Hasse*, 1992; *Caulliez* 1998; *Melville et al.*, 1998; *Veron and Melville*, 2001; *Sanjou et al.*, 2011]. It has been shown that LC-induced cold streaks on the water surface do not appear before the onset of surface waves and only at critical Reynolds numbers. *Melville et al.* [1998] found that LCs scale with the depth of the shear layer and observed a spanwise scaling of l_c = 5.42 cm. Measurements conducted by *Sanjou et al.* [2011] indicate the significance of wind speed on the spacing of the Langmuir vortices. *Mizuno* [2011] observed Langmuir circulations in a linear wind wave channel that were destroyed by additional mechanical waves, thereby contradicting CL II theory.

[23] In this contribution, a novel method is presented for the analysis of footprints of near-surface turbulence. This approach is based on image processing and machine learning methods. The spacing of cold surface streaks is related to wind speed and surface conditions. The characteristic features of the heat pattern are distinguished according to their scales. The detection of the small-scale streak spacings is done on the infrared images. The spacing of Langmuir circulation on the other hand is determined from the temporal images (see Figure 1). It was possible to automate the streak detection process and analyze large amounts of experimental data.

2. Analysis of the Surface Heat Pattern

[24] Our goal is to achieve a full segmentation of the surface heat pattern, e.g., classifying each pixel as part of a (cold surface) "streak" or "no streak." Therefore, a classification method is needed based on features of the image. The easiest method would be a simple temperature threshold, classifying pixels colder than this threshold value as "streak" and those warmer as "no streak." Due to temperature variations on several scales, a simple temperature threshold is not sufficient to achieve a segmentation of the surface heat pattern (see Figure 3).
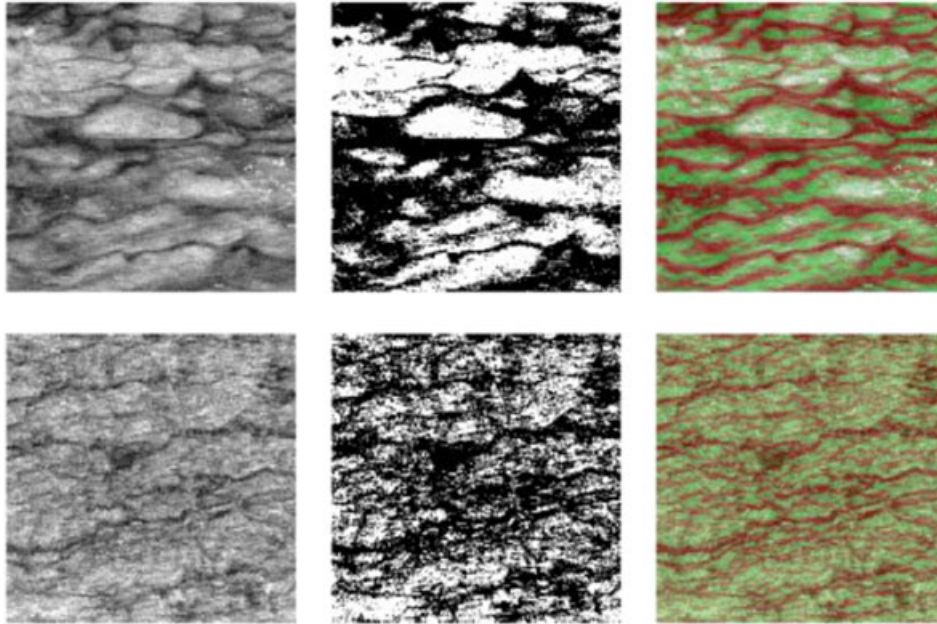
Figure 3. Infrared images (Aeolotron) of the water surface at two different wind speeds (left column); simple temperature threshold (middle column); result of the classification process (right column); red, "streak;" green, "no streak."

2.1. Pixel-Based Segmentation

[25] Our approach is a machine learning-based algorithm which uses a random forest classifier [*Sommer et al.*, 2011]. The classification does not rely on one feature (for example temperature) but several features, which is a big advantage in the case of the highly variable surface heat pattern. The second advantage is the high flexibility of this detection mechanism. The classifier is "taught" (by labeling) which combination of features most probably describes a class ("streak" or "no streak") and later uses this training data to classify pixels (see Figure 2 for algorithm description).

[26] The random forest is based on classical features in image processing such as gray value gradients and edge-detecting features. A supervised learning process can be chosen because features can be selected from the characteristic shape of the surface heat pattern (e.g., cold streaks are oriented in wind direction, step edges appear along the streaks, etc.).

[27] The first step of the analysis is to choose appropriate features that describe the observed heat pattern, obviously such as gray value, edge, and orientation. Then, the corresponding scale on which the filters operate is chosen, and these are the features on which the random forest classifier is based. M is the number of features which are chosen to describe the given problem. This means that for every image, there are M images that contain the values of the selected features at every pixel.

[28] The random forest classification method used here follows *Breimann* [2001]: The user manually labels a set of N pixels. To every labeled pixel belongs a number of feature values. This is called a feature vector that contains the values of the previously selected features at the location of the labeled pixel.

[29] From the labeled feature vectors, $n \ll N$ are chosen randomly (with replacement) and represent the so-called bootstrap sample. Now, a number of features $m \ll M$ are randomly selected to divide the bootstrap sample into two subsets. This is repeated with every subset until the classes ("streak" and "no streak") have been entirely separated—and one decision tree is grown. The so-called random forest consists of a number of decision trees and their average "vote" is decisive for the classification of a pixel. Once the random forest is generated from the training images, it can be used to classify all other (unlabeled) images. So every image follows the structure of the constructed random forest.

[30] The result is a pixel-wise classification of the surface heat pattern. Therefore, no spatial patterns or global correlations are accounted for in the probability maps.

[31] As a measure of variable importance, we used the maximum mean Gini increase, which is a measure of the importance a variable has on the decision in each node of a decision tree. The comparison of Gini gains for low wind speeds yields the feature "orientation" based on the the structure tensor and entries of the Hessian matrix on a scale of $\sigma = 3.5$ as the most important variable. Followed by edges, which is based on eigenvalues of the structure tensor and Hessian matrix as well as gradient filters such as difference of Gaussians and Laplacian of Gaussian. Finally, the gray value intensity, which is based on a first smoothing on scales of $\sigma = 0.3 - \sigma = 3.5$. For higher wind speeds, features remain the same but there is a shift to smaller filter scales which corresponds to the visible change of the surface heat pattern to smaller structures.

[32] Four statistically independent images from each recorded condition present the basis of the following training and classification process and were labeled manually. The algorithm was trained independently on the data of the different measurements and subdivided into wind speeds.

Cases of clean water and surfactant covered water surface were treated as one condition.

[33] Three distinct classes, "streak," "warm plume," and "reflexion" (resulting from the cold camera chip surrounded by the camera window), are chosen to describe the surface heat pattern. The result of the classification is a probability map which shows the calculated probability for a pixel of being a "streak" or not (Figure 3, column 3).

[34] The quality of the resulting classification has been carefully surveyed. Unfortunately, there is no "ground truth" to which the classification results could be compared. Therefore, cold surface streaks were marked manually and this result was compared to the result obtained during the data analysis for this specific image. This approach showed good agreement and leads to an error of 6.4% wrongly classified pixels at low wind speeds to 15% at high wind speeds. Additionally an optimal probability map of one image was generated by using a very high number of manually marked pixels and subsequently compared to a classification of the same image with the standard random forest. This leads to an error of 7% for wrongly classified pixels at low wind speeds and 10% at high wind speeds. Here, mainly the boundary areas of the streaks cause the error but not the center which determines the spacing. Another source of errors is the variable environment of the water surface and depends strongly on measurement conditions. Under certain conditions (see section 3.2), microscale breaking waves are present.

2.2. Analysis of the Streak Spacing

[35] For the last step of the analysis, e.g., the extraction of the streak spacing, we chose statistically independent probability maps. The streak spacing is determined from the center of one streak to the center of the next on a line in cross-wind direction. To ensure that the measured spacings are not spatially correlated as they would be if the spacing was determined from two successive lines, only two lines with a sufficient distance of each of the selected probability maps were picked. The determination of the centerline of the streak is accurate on pixel level and based on the segmented image.

[36] A log normal distribution describes the histograms of measured streak spacings very well. Therefore, a log normal function is fitted to the data, and its features form important parameters to compare the results for different wind speeds and surface conditions.

[37] In the regime of small streak spacings, irregular edges of the segmented images and wrong detections due to overlapping classes lead to a slightly higher number of very small streak spacings than expected. Streak spacings of such a small scale have not been observed in the images and are therefore not considered physical. The error is comparatively small and does not disturb the log normal fit.

[38] In the spilling region of a microscale breaking wave, the surface heat pattern is wiped out as surface renewal takes place. In this region, no streak spacings are detected. This does not influence the distribution of spacing as incoherent turbulence does not lead to any structures that could accidentally be taken for streaks. However, it leads to gaps that lead to a slight overestimation of very large spacings. For these reasons, the position of the mode was selected as the most reliable feature of the distribution to characterize the streak spacing.

3. Measurements

[39] The data presented here were measured in three facilities, the Aeolotron, Heidelberg, the Water Research Laboratory, Sydney, and the Air Sea Interaction Saltwater Tank, Miami. Therefore, a comparison of surface heat patterns under very different experimental conditions and recorded with different imaging systems is possible. In the following, these experiments are each individually described.

3.1. Aeolotron, University of Heidelberg

[40] The experiments were conducted at the circular wind wave facility at the Institute for environmental Physics in Heidelberg (IUP).

[41] The water depth was kept constant at (1.00 ± 0.01) m throughout the experiment. The diameter of the tank is 10 m with a perimeter of 29.2 m. The width and height of the channel are 61 cm and 2.30 m, respectively.

[42] Two fans within the air space on opposite sites produce wind up to a wind speed of 12 m/s.

[43] The channel can be operated with closed doors and a closed air space to minimize the latent heat flux (relative humidity of the air reaches ~100%). The walls of the channel are insulated by a 9 cm layer of polystyrene to reduce sensible heat flux and the walls are covered with aluminum foil to minimize radiative heat flux. During the measurements with passive thermography, for which the development of a cool surface layer is crucial, the channel was operated with an additional ventilation that circulated dry air from outside through the channel. Therefore, relative humidities were reduced to an approximately constant 60%.

[44] The wind speeds in this experiment ranged from 1 up to 6 m/s 1 m above the water surface. Mean square slope (MSS) values were obtained from the color imaging slope gauge (CISG) as described in *Rocholz et al.* [2011]. The water-sided friction velocity was calculated from the momentum budget in the channel [*Bopp*, 2011]. For this purpose, bulk water velocities were measured, and the decay characteristics of the velocity of the water body after stopping the wind were determined from the spin-down time.

[45] The measurements were repeated after adding 3 g Triton X-100. Triton X-100 is a surfactant that has a hydrophilic polyethylene oxide group which makes it soluble in water. By the reduction of surface tension, it effectively suppresses capillary waves. To study the influence of capillary waves on the surface heat pattern, all wind conditions were repeated with a surface slick. As as result, mean square slope values were close to zero for the low wind speed cases and the heat flux reduced in comparison to clean surface measurements (see Figure 9 and Table 1 and 2 for experimental conditions).

[46] The employed infrared camera is a Thermosensorik CMT 256 with a resolution of 256×256 pixel (px) and a maximal frame rate of 880 Hz. The frame rate during the measurements was reduced to 60 Hz as a higher time resolution was not necessary. The temperature resolution of the camera amounts to 10 mK. The camera is sensitive to radiation in the range of 3.4–5.1 μm. The camera is mounted on top of the wave channel approximately 1.30 m

Table 1. Aeolotron, Thermosensorik CMT 256[a]

U	u^*	MSS	Heat Flux
1.8	0.20	0.014	170
2.4	0.33	0.017	170
2.7	0.34	0.024	181
4.6	0.77	0.049	219
6.4	1.36	0.082	246

[a]In Tables 1–4, U, u^*, MSS, and heat flux are the wind speed in meters per second, the friction velocity in centimeters per second, the mean square slope values, and the total heat flux in watts per square meter, respectively. The measurement error of the friction velocity is 0.02 cm/s for low and intermediate wind speeds and 0.1 cm/s for the highest wind speed. The values for the heat flux are mean values for the respective wind speed.

Table 2. Aeolotron, Surfactants (Triton X-100), Thermosensorik CMT 256

U	u^*	MSS	Heat flux
1.8	0.18	0.005	142
2.4	0.25	0.005	142
3.4	0.40	0.008	158
4.6	0.64	0.010	169
6.4	1.35	0.045	186

above the water surface. To obtain a better spatial resolution, a lens with a focal length of 50 mm was utilized. The spatial calibration with a target with a checkerboard pattern on the water surface yielded a spatial resolution of 0.1135 ± 0.0006 cm/px.

[47] The temperature calibration of the camera was performed in the range of 15°C–24°C in steps of 0.25°C. For this purpose, a reference calibration blackbody was set to the respective temperatures, an infrared image was recorded of each temperature and subsequently used for the calibration of the camera. Sequences with 1000 images ($\sim$16 s) each were recorded for 20 min, resulting in 50 sequences and 50,000 infrared images.

[48] The clean surface measurements were again repeated with a new IR camera, an IRCAM Velox 327k M, which has a resolution of 640×512 px. The spatial resolution amounts to 0.0778 ± 0.0006 cm/px during the experiment which is considerably higher than in the previous measurement. Hereby it is ensured that the resolution of the camera does not effect the analysis of the streak spacing.

3.2. Water Research Laboratory, University of New South Wales

[49] The wind channel used for the experiments is a linear channel. The tank is 8.955 m long, 0.245 m wide, and 0.610 m high. A detailed description of the experiments can be found in *W. L. Peirson et al.* (On the microphysical behaviour of wind-forced water surfaces and consequent re-aeration, submitted to *Journal of Fluid Mechanics*, 2013). All technical data and experimental conditions were taken from this study.

[50] The water depth during the experiments was 0.247 m $\pm$ 1 mm. The wind was produced by a ventilator at one end of the tank. To ensure a uniform airflow, guide vanes were installed just behind the ventilator. The tank is located in an insulated room at constant temperature of 21.5 ± 0.5°C throughout the experiment.

[51] As wind-generated and surface conditions in a linear tank are fetch dependent, the wind and wave conditions were chosen so that constant wave energy levels were obtained for the entire fetch length. To avoid biological activity, the water was steadily circulated through an Earth filter and UV sterilizer, when no experiments were performed.

3.2.1. Wind Wave Conditions

[52] Mechanical waves were produced by a paddle at one end of the tank. During the experiments measurements were conducted under eight different wind wave conditions (see Table 3).

[53] Two *low wave cases* (F34U21AK18 and F21U39AK10) were performed at a fetch of 4.55 and 3.1 m and therefore different wave characteristics at $U_{10} = 2.1$ and 3.9 m/s, respectively. The numbers F34U21AK18 and F21U39AK10 describe wave frequency, wind speed, and the value of *ak*. Here F34U21AK18, for example, stands for a wave frequency of 3.4 Hz, a wind speed of 2.1 m/s, and a value of $ak = 0.18$. The low gravity waves were mechanically produced with a length 135 and 350 mm. The steepness of the waves was low enough that no parasitic capillary waves could evolve.

[54] Two *incipient breaking cases* (F34U21AK27 and F24U39AK24) were also performed at a fetch of 4.55 and 3.1 m at wind speed of $U_{10} = 2.1$ and 3.9 m/s. Incipient breaking refers to waves as steep as possible before the onset of microscale breaking. Here parasitic capillary waves were present.

[55] Two *microscale breaking cases* (F34U57AK32 and F31U39AK28) were also performed at a fetch of 4.55 and 3.1 m. Wind speeds were $U_{10} = 5.7$ and 3.9 m/s as microscale breaking could not be maintained for $U_{10} = 2.197$ m/s.

[56] The *capillary ripple case* (F63U42AK00) was performed at a fetch of 3.1 m with freely propagating capillary waves present. The wind speed was $U_{10} = 4.2$ m/s, and no gravity waves developed.

[57] The *flat water case* (F00U21AK0) was performed at a fetch of 4.55 m. The wind speed $U_{10} = 2.1$ m/s was the highest possible wind speed without the formation of freely propagating waves.

[58] A wave probe recorded the surface elevation at 1 kHz. Additionally Particle Image Velocimetry (PIV) and Laser Induced Fluorescence (LIF) measurements were performed, the detailed description of which can be found in Peirson et al. (submitted manuscript, 2013) and will not be further discussed in this study. The infrared camera was a cedip Jade 550, operated at a frame rate of 100 Hz with a resolution of 320×240 pixels. The camera was mounted

Table 3. Water Research Laboratory[a]

U	u^*	ak	f
2.1	0.45	0.18	3.4
2.1	0.75	0.27	3.4
5.7	1.81	0.32	3.4
4.2	0.62		6.3
3.9	0.81	0.10	2.1
3.9	1.11	0.24	2.4
3.9	1.46	0.28	3.1

[a]The wave steepness and the wave frequency in hertz are given by ak and f, respectively.

Table 4. ASIST Facility

U	u^*	Heat flux
1.9	0.22	393
3.0	0.31	601
4.0	0.43	850
5.0	0.57	1144
7.0	0.93	1764
10.1	1.65	2592

on top of the channel looking down on the water surface with the wave probe visible. The spatial calibration using the wave probe as a target yielded a spatial resolution of 0.066 ± 0.002 cm/px. The data were recorded in two independent sequences of 4996 images for every experimental condition.

3.3. Air-Sea Interaction Saltwater Tank, Rosenstiel School of Marine and Atmospheric Sciences

[59] The experiments were performed at the Air-Sea Interaction Saltwater Tank (ASIST) located at the University of Miami (Rosenstiel School of Marine and Atmospheric Science) and are described in detail in *Smith et al.* [2007].

[60] The linear tank is 15 m long, 1 m wide, and 1 m high. The water depth during the experiment was 40 cm, leaving 60 cm for the wind. For all the cases presented here, a water pump was used to maintain a small, constant current (approximately 3 cm s^{-1}) that enabled control of the water temperature. Water temperatures were varied to provide air-water temperature differences ranging from –15°C to +15°C. Wind speeds were varied from 0 up to 10 m s^{-1}. All cases presented here are cool-skin cases, e.g., the heat flux was directed out of the interface (see Table 4 for heat flux values).

[61] The infrared images were taken with an Indigo Systems Merlin Mid-Wave IR sensor with a resolution of 320 × 256 pixels. The spatial resolution of the images amounts to 0.0907 cm/pixel. The array is cooled to increase sensitivity to better than 0.02°C. The imager is sensitive to radiation in the 3–5 μm band. The maximum frame rate of the IR imager is 60 Hz, although the actual acquisition rate was varied based on the flow being imaged. All the imagery were taken looking down at the water surface at an angle of approximately 60°from the horizontal through a hole in the top of the tunnel. This was done for two reasons: first to reduce the occurrence of reflections of the camera itself appearing in the data and second to accommodate a second IR imager viewing through the same port in the roof of the wind wave tunnel. Additionally the camera was oriented diagonally to the wind direction.

4. Results

4.1. Small-Scale Turbulence-Induced Streak Spacing

[62] We have applied an image processing-based approach to determine the spatial scales of shear-induced turbulence to data measured in wind wave facilities in Heidelberg, Sydney and Miami. In the obtained images, regions of surface divergence and convergence are visualized as warm (light) areas, where bulk water bursts into the water surface, and cool (dark) areas, where surface convergence zones evolve. In all images a characteristic heat pattern appears, termed fish scales by *Handler et al.* [2001] and *Tsai et al.* [2005]. Their terminology is adopted here. The temperature difference between warm and cold areas amounts to ∼0.4 K for lower wind speeds and clean water conditions and ∼0.3 K for cases with surfactants present.

[63] A comparison of infrared images from the three different facilities is shown in Figure 4. Figure 4a was taken in the Aeolotron, Heidelberg, with a spatial resolution of $res = 0.11$ cm/px and at a friction velocity of $u^* = 0.8$ cm/s. Figure 4b was taken under the same conditions in the same tank but with a spatial resolution of $res = 0.07$ cm/px. In Figure 4c, an image from WRL, Sydney, is shown, which was recorded with a spatial resolution of $res = 0.07$ cm/px at a friction velocity of $u^* = 1.1$ cm/s. In the image, a laser-heated spot is clearly visible but could easily be identified over its temperature and did therefore not further influence the analysis. Figure 4c is from the ASIST facility, Miami, the spatial resolution is $res = 0.09$ cm/px and the friction velocity is $u^* = 0.9$ cm/s. The camera was oriented diagonally to the wind direction. Therefore, the images are rotated in such a way that the fish scale structures lie in the horizontal axis and a rectangular window aligned with the structures was cut (Figures 4d and 4e). This was necessary to avoid a suppression of larger scale spacings in the corners of the image.

[64] In Figures 5 and 6 below, representative infrared images of the water surface are shown that were taken during this study at the wind wave facility Aeolotron, Heidelberg. Figure 5 shows the heat pattern on a clean water surface, Figure 6 shows the heat pattern on a surfactant-covered water surface. In both figures, results are shown at four different wind speeds, from low to moderate. The friction velocity increases from approximately 0.14 to 0.77 cm/s. Comparing Figures 5 and 6, a strong similarity becomes evident even though nearly no waves were present in the surface slick cases (compare Figure 9).

[65] Red bars in Figures 5 and 6 indicate the size of the obtained mean streak spacing, blue bars in comparison theoretical values for flow near a no-slip wall. For the higher wind speeds both bars are of approximately the same size which indicates a similar turbulence production process even though the physical conditions are different (no-slip versus free-slip boundary conditions). However, for low wind speeds, the observed spacings are significantly smaller. In those cases, the surface Richardson number is below the critical value suggested by *Soloviev and Schlüssel* [1994]. This indicates that at the lowest wind speeds in Figures 5 and 6, free convection is the dominant process. For higher wind speeds a transition takes place and the turbulent cell size matches that of shear induced turbulence. However, for friction velocities above $u^* = 0.7$ cm/s, observed spacings are significantly higher than the continuously decreasing theoretical values for shear-induced turbulence (see Figure 8).

[66] The analysis of the fish scale pattern yields a logarithmic distribution of streak spacings. In Figure 7, the obtained distributions are shown at four different wind speeds (same conditions as in Figure 5) and a clean water surface. With increasing wind speeds, the mean spacings are clearly shifted to smaller values and the standard deviation
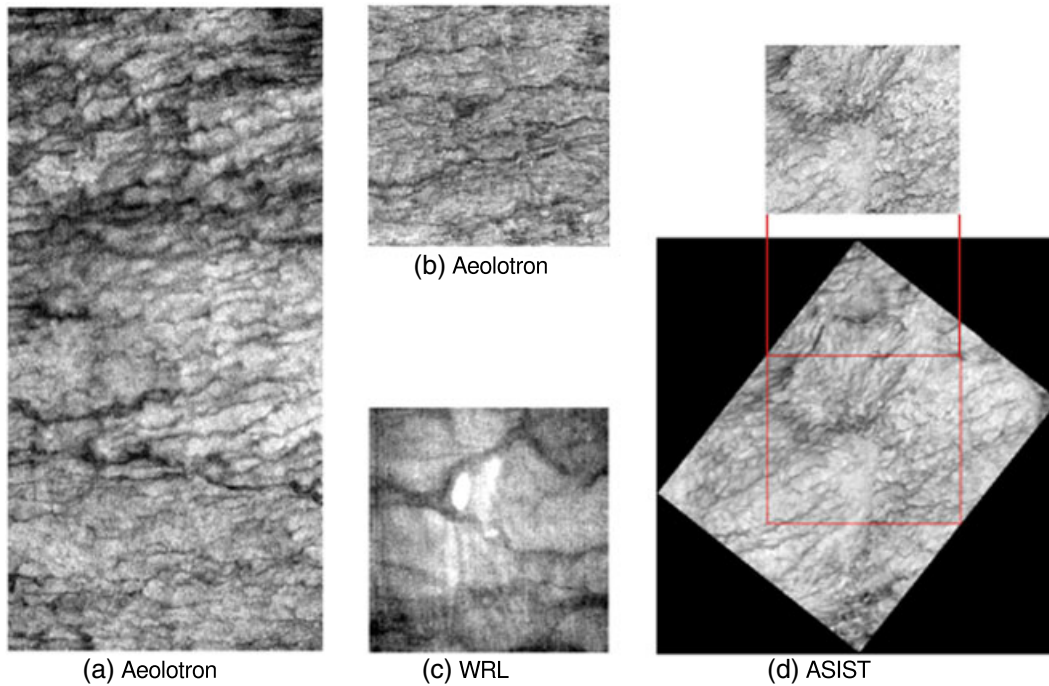
Figure 4. Infrared images from several facilities. The images were recorded with different IR cameras and different spatial resolution (*res*): (a) Aeolotron, Heidelberg, Thermosensorik CMT 256, *res* = 0.11 cm/px, $u^* = 0.8$ cm/s; (b) Aeolotron, Heidelberg, Ircam Velox 327k M, *res* = 0.07 cm/px, $u^* = 0.8$ cm/s; (c) WRL, Sydney, cedip Jade 550, *res* = 0.07 cm/px, $u^* = 1.1$ cm/s, a warm laser-heated spot is clearly visible in this image; and (d) ASIST, Miami, Indigo Systems Merlin, *res* = 0.09 cm/px, $u^* = 0.9$ cm/s, the originally image is rotated and a rectangular section cut for the analysis.

σ decreases (see Table 5). A log normal distribution evolves, if the random forces that act on the random variable are proportional to the variable. This indicates that forces that cause the formation of the streaks are in some way proportional to the streak spacing [*Smith and Metzler*, 1983]. The observed logarithmic distribution of streak spacing has previously been described by *Tsai et al.* [2005] obtained from the numerical simulation of a flat water surface and the spacing of low speed streaks near a no-slip wall measured by *Smith and Metzler* [1983] indicating the similarity of the process.

[67] This is qualitatively consistent with the description of the features of the fish scale pattern described by *Tsai et al.* [2005].

4.1.1. Correlation of Streak Spacing and Friction Velocity

[68] The modes of the fitted log-normal distributions of all the experiments that are accounted for in this work are shown in Figure 8. The error bars mark the 1σ confidence interval of the log normal distribution which illustrates the variability of the obtained statistics but not the measurement error. The error bars of u^* represent the measurement errors and depend on the measurement technique.

[69] It is remarkable that the measured streak spacings do not vary by more than 30% even though the data were collected under several entirely different experimental conditions such as clean water surface, surfactant-covered water surface, a cooled and heated water body resulting in warm and cool skin cases, and additional mechanical waves. However, the data from the wind wave channel at WRL show constantly slightly higher values of streak spacing in comparison to the other cases. Also the histograms of the spacing scatter far more (and have therefore a higher error) and show a broader distribution. Partly this can be explained by the additional surface waves along with resulting disturbances of the surface heat pattern. Additionally a considerably smaller heat flux leads to less prominent cold surface streak and may cause an overestimated spacing if small streaks cannot be detected.

[70] The streak spacing does not seem to be influenced either by the presence of surfactants or by the presence of additional mechanical waves. Even though surfactants have the above mentioned effects on near surface turbulence and lead to a damping of turbulence [*Soloviev et al.*, 2011], it does not seem to influence the spacing of the evolving streaks.

[71] The expected lapse of streak spacings from experiments and simulations of low speed streaks near no-slip walls over u^* would be continuous ($l^+ = lu^*/\nu = 100$). The distribution of streak spacings over u^*, that was obtained in this analysis shows a different behavior. At friction velocities up to a value of 0.7 cm/s, there seems to be a clear trend of smaller spacings at larger u^*, and in this regime, the development could be described by a linear regression. So in regimes of small friction velocities, there seems to be a clear link between the size of the turbulent structures and the tangential shear stress producing them.

[72] This behavior changes at a friction velocity of approximately 0.7 cm/s. From this point on, streak spacings remain approximately constant and are seemingly independent of u^*.
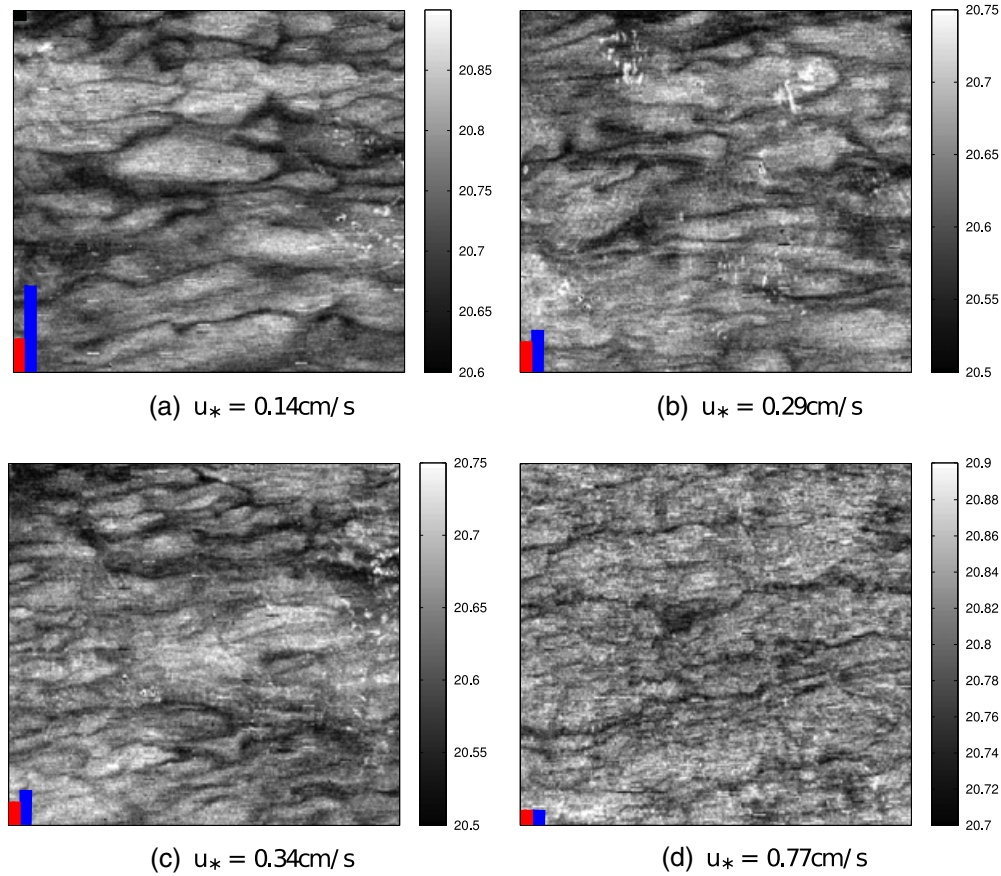
Figure 5. Thermographic images of the water surface at four different wind conditions. The images were taken at the Aeolotron, Heidelberg. The red line represents the size of $\overline{\lambda_{exp}} = \overline{l_{exp}}u^*/\nu$, where l is the determined mean streak spacing for each case, u^* the friction velocity and ν the kinematic viscosity. The blue line represents in comparison the size of $\overline{\lambda_{theo}} = 100u^*/\nu$ for the value of the mean dimensionless streak spacing of $l = 100$ which would be expected in the case of low speed streaks near a no-slip wall.

[73] There seems to be a lower boundary for the size of the coherent turbulent structures as the spacing of the streaks is a direct measurement of the width of the shear-induced turbulence and therefore also of the same scale as the shear layer itself [*Hunt et al.*, 2011]. One possible explanation is the saturation of tangential stress at the water surface above a threshold friction velocity u^*.

[74] There is also a lower boundary for the size of the structures that can still be detected. But similar values for measurements with infrared cameras with different spatial resolutions and therefore different lower detection boundaries show that this is probably not the reason for the stagnating streak spacings.

[75] *Banner and Peirson* [1998] found that the increase of tangential stress with wind speed is limited. The relation of tangential to total wind stress (τ_t/τ) has a trend toward a value of 0.3. With increasing wind stress an increasing part of the total wind stress is transformed into wave form drag while the tangential stress is even slightly decreasing [*Banner and Peirson*, 1998]. This effect might well be an explanation for the here observed stagnating streak spacing. The transition of streak spacing into the plateau corresponds to the *Banner and Peirson* [1998] observed wind speed and the appearance of the first gravity waves.

[76] Interestingly the stagnation point is reached at approximately the same u^* for all experimental conditions including different fetches and even experiments with surface slicks. In the cases with surface slicks, it should be noted that in all data points that are in the stagnating area, gravity waves were present at MSS values of the same magnitude (approximately 70%) as in the cases without slicks (compare Figure 9).

[77] There seems to be a slightly larger variation within the streak spacings obtained at UNSW with additional mechanical waves. This could well be the case because of variations in the shear stress coherent with the phase of the underlying mechanical waves.

4.1.2. Influence of Wave Conditions

[78] It has been shown that the wave field has no (or very small) influence on the distribution of streak spacing. However, there seems to be a small variation of the streak spacing along the wave phase. The results are obtained from the data measured in a linear wind channel at the Water Research Laboratory (WRL) at the University of New South Wales (UNSW). The wave height was measured with a wave probe which was also visible in the infrared images. From the known position of the heated spot and the knowl-
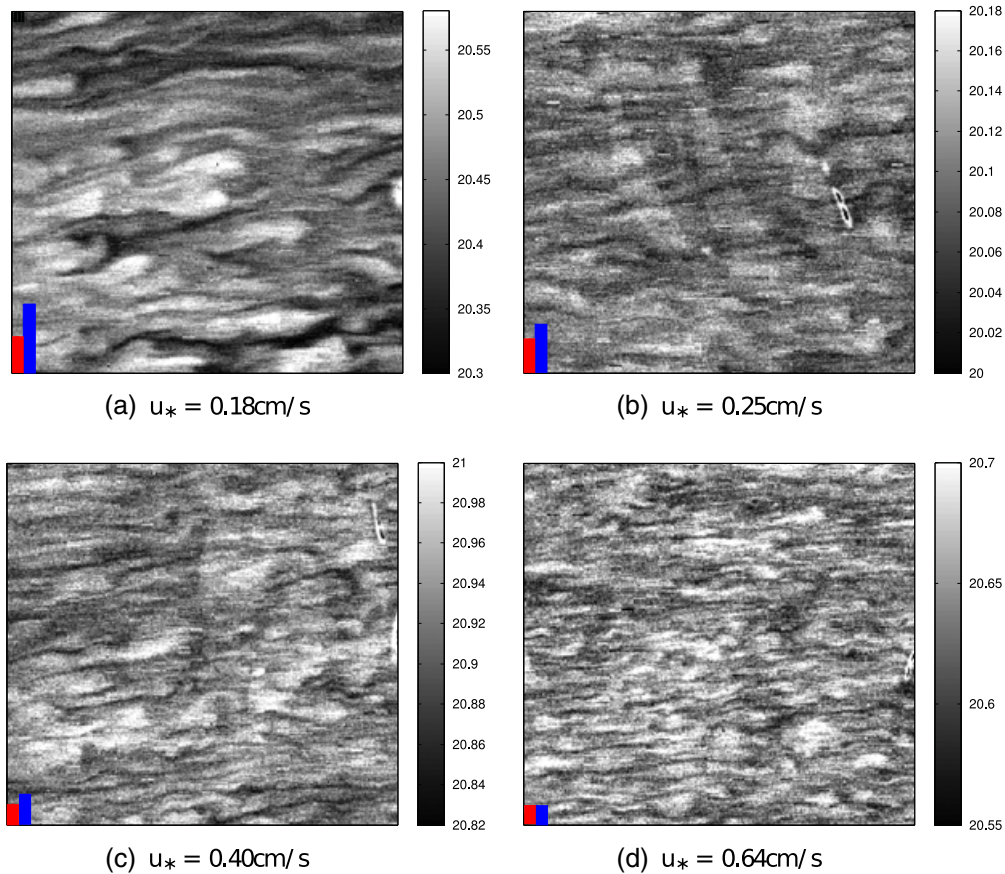
Figure 6. Thermographic images of the surfactant (Triton X-100) covered water surface at four different wind conditions. The images were taken at the Aeolotron, Heidelberg. The red line represents the size of $\overline{\lambda_{exp}} = \overline{l_{exp}} u^*/\nu$, where l is the determined mean streak spacing for each case, u^* the friction velocity, and ν the kinematic viscosity. The blue line represents in comparison the size of $\overline{\lambda_{theo}} = 100 u^*/\nu$ for the value of the mean dimensionless streak spacing of $l = 100$ which would be expected in the case of low speed streaks near a no-slip wall.

edge of the wave phase, it was now possible to calculate the mean spacing at the position of the heated spot in one line of the image. In Figure 10, an average of the obtained mean streak spacings is plotted against the wave phase. In the incipient breaking case with a u^* of 1.1 cm/s, there is a small increase to larger streak spacings just behind the wave crest. A similar distribution could have been expected because of the crucial role that shear stress plays in the development of the small-scale heat pattern. *Peirson* [1997] and *Banner and Peirson* [1998] found the tangential shear stress to decrease from the wave crest at 0°to nearly zero at approximately +75°. This corresponds to the wave phase in which the increase of streak spacing was observed. This is consistent with the assumption of the small-scale turbulent structures being shear induced. In this regime of moderate wind speeds, a decreased shear stress leads to larger streak spacings for sufficiently small friction velocities.

4.2. Langmuir Circulation-Induced Cold Streaks

[79] Larger-scale streaks evolve in the cases of higher wind speeds (compare Figure 5). These seemingly stable turbulent structures indicate the presence of Langmuir cells. In this section the influence of surface conditions

like surfactants and waves on the development of stable Langmuir-like turbulent structures will be examined.

[80] To be able to separate more stable structures from the more instable ones, it is instructive to regard the temporal development of the turbulent structure. Therefore, one line at fixed position perpendicular to the wind direction was taken from each image of a recorded sequence (compare Figure 1). In this time-based depiction, it is possible to separate the more unstable shear-induced turbulence from the apparently very stable Langmuir-like circulation that stretches over several wave periods. The resulting Figures 11 and 12 show the behavior of near-surface turbulence at a given spatial position in a time interval of ∼16 s in Figures 11 and 12.

4.2.1. Influence of Surface Conditions on Langmuir-Like Turbulent Structures

[81] Comparing the results of the clean water surface with those of a surfactant covered water surface, a striking difference between the small-scale heat pattern and the larger-scale Langmuir circulations becomes evident. The larger-scale cold streaks only appear in the cases of a clean water surface while the fish scale pattern is universal. At increasing wind speeds, these larger-scale streaks with a
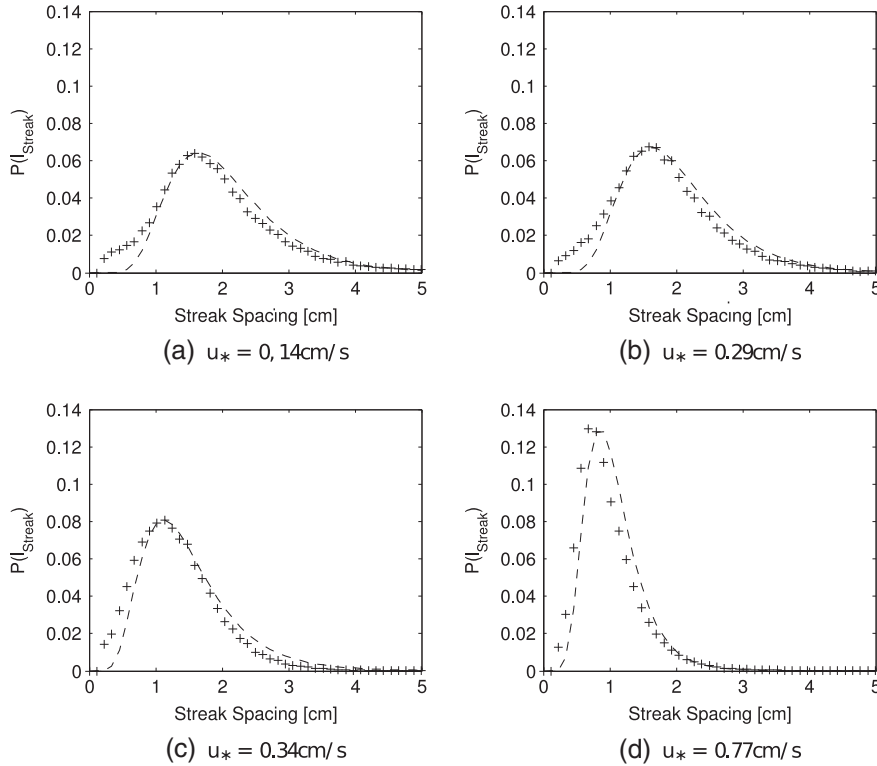
Figure 7. Histograms of obtained streak spacings at four different friction velocities with a log normal fit on the data, Aeolotron, Heidelberg, clean surface conditions.

spacing of approximately 8–12 cm become more and more pronounced. For higher wind speeds, the circular geometry of the wave channel Aeolotron causes a deflection of the orientation, and the cold surface streaks run slightly diagonally. In the cases of surfactants on the water surface, only the familiar fish scale pattern evolves but no signs of any larger-scale circulation.

[82] This is consistent with the CL II mechanism of an interaction of shear stress and waves *Craik and Leibovich* [1976] and has previously been observed by *Caulliez* [1998] and *Veron and Melville* [2001].

4.2.2. Influence of Mechanical Waves on Langmuir-Like Turbulence

[83] In the data set measured at Water Research Laboratory at UNSW the influence of mechanical surface waves at different wave conditions and wind speeds on micro-Langmuir circulations becomes evident.

[84] Langmuir circulation indicating cold streaks occur in all cases except for the strongest breaking case. They are clearly present in the capillary ripple cases. They are less distinct in the low wave cases but can clearly be seen in the incipient breaking cases and in the microscale breaking case for lower *ak* values. In the microscale breaking case with a value of *ak* = 0.32, there are no more stable circulations visible.

[85] *Mizuno* [2011] observed similar behavior of Langmuir cells under the presence of mechanical waves. Langmuir circulations in a linear wind wave channel were destroyed by additional mechanical waves, thereby contradicting CL II theory. The suggested explanation is that the additional energy introduced by mechanical

waves enhances the wave growth without leading to an enhanced wave breaking which would lead to a dissipation of the energy. Therefore, it is concluded in *Mizuno* [2011] that an enhanced return flow leads to a collapse of the Langmuir vortices. This effect was found to appear at values of *ak* = 0.1. In these measurements, the dark streaks indicating stable Langmuir circulations persist until values of *ak* = 0.32.

4.2.3. Langmuir Numbers and Streak Spacings

[86] From the temporal profiles, the streak spacings have been estimated in the cases in which the streak spacing was small enough to be captured by the image size.

[87] The conditions during the measurements at WRL (monochromatic waves with a set frequency *f*, wave number *k*, and amplitude *a*) allow a comparison with the LC stability theory developed by *Leibovich and Paolucci* [1981]. This is done in analogy to *Melville et al.* [1998]. The stability theory applies for a homogeneous stationary wave field with wind beginning at a certain time with constant stress.

[88] The Langmuir number is calculated according to equation (3).In analogy to *Melville et al.* [1998], the eddy viscosity is estimated from the shear layer thickness. As the shear-induced turbulence scales with the shear layer thickness [*Hunt et al.*, 2011], the scale obtained from the analysis of the small scale shear induced turbulence is used for the estimation of the eddy viscosity.

$$\nu_t = ku^* l_{\text{S.I.T}} \qquad (4)$$

with the von Karman constant $k = 0.4$, the spacing of the shear-induced turbulence $l_{\text{S.I.T}}$, and the friction velocity u_*.

Table 5. Summary of the Analyzed Streak Spacings and Experimental Conditions[a]

Aeolotron, No surfactants				Aeolotron, Surfactants (Triton X-100)			
U	u^*	Spacing	Sigma	U	u^*	Spacing	Sigma
1.0	0.13	1.59	0.06	1.8	0.18	1.70	0.06
1.2	0.14	1.59	0.04	2.4	0.25	1.36	0.04
1.8	0.20	1.48	0.05	2.4	0.25	1.56	0.04
2.6	0.29	1.48	0.05	3.4	0.40	1.25	0.05
2.4	0.33	1.48	0.04	3.4	0.40	1.02	0.05
2.7	0.34	1.13	0.05	4.7	0.65	0.91	0.04
2.4	0.29	1.02	0.05	4.6	0.64	0.68	0.04
4.6	0.77	0.68	0.04	6.5	1.04	0.79	0.04
4.6	0.77	0.79	0.04	6.4	1.02	0.91	0.06
6.4	1.36	0.91	0.04				

ASIST, Miami				WRL, Sydney			
U	u^*	Spacing	Sigma	U	u^*	Spacing	Sigma
1.9	0.21	1.31	0.04	2.1	0.45	1.3	0.1
2.9	0.31	1.14	0.04	2.1	0.75	1.2	0.1
4.0	0.43	0.85	0.04	5.7	1.81	1.0	0.1
4.0	0.44	0.90	0.04	4.2	0.62	1.1	0.1
5.0	0.58	0.73	0.04	3.9	0.81	1.0	0.1
5.0	0.57	0.69	0.04	3.9	1.11	1.2	0.1
7.1	0.93	0.69	0.04	3.9	1.46	0.8	0.1
10.1	1.65	0.69	0.04				

[a] The streak spacing of the small-scale turbulence results from the log normal fits on the obtained distributions. U, u^*, MSS, streak spacing, and sigma are the wind speed in meters per second, the friction velocity in centimeters per second, the mean square slope values, the streak spacing as the result of the analysis in centimeters, and the standard deviation of of the distribution of the streak spacing also in centimeters, respectively. The measurement error of the friction velocity is 0.02 cm/s for low and intermediate wind speeds and 0.1 cm/s for the highest wind speed. Sigma can be seen as a measure of the variability of the log normal distributions of spacing.

[89] Both *Leibovich and Paolucci* [1981] and *Melville et al.* [1998] presented a stability diagram of dimensionless wave numbers $k^*_{LC} = k_{LC}/k_{wave}$ against inverse Langmuir numbers La^{-1}. Here k_{LC} is the "wave number" obtained from the spacing of Langmuir streaks and k_{wave} is the wave number of the mechanically generated waves. The inverse Langmuir number can be regarded in analogy to the Rayleigh number. The Rayleigh number describes the relationship between buoyancy and viscosity in the case of heat convection. Accordingly, La^{-1} describes the quotient of inertial and viscous forces in CL II theory.

[90] Consequently, the flow is stable for very small La^{-1} and becomes unstable for larger La^{-1}. In Figure 13, the data points obtained here are compared to the global stability boundary that is found for constant Richardson numbers ($Ri = 0$) while varying Langmuir number La and wave number k [*Leibovich and Paolucci*, 1981] and the values obtained by *Melville et al.* [1998]. The global stability boundary developed by *Leibovich and Paolucci* [1981] is derived from the time of the onset of instability. The measurement of *Melville et al.* [1998] are correspondingly made at the onset of Langmuir circulations. In contrast, the values obtained here originate from an equilibrium state with both, wave field and wind stress constant in time. A comparison still shows good agreement. The obtained values for La^{-1} are located in the unstable regime as expected.

[91] The large error bars arise mainly from the inaccurate determination of the streak spacing. Wavelength for the data measured at the Aeolotron has been determined from the images of the CISG in the low wind speed case and for the case with a higher wind speed from the new experimental measuring technique for the characteristics of gravity waves of *Eisenhauer* [2011]. *Melville et al.* [1998] measured growing La^{-1} numbers prior to the inception of
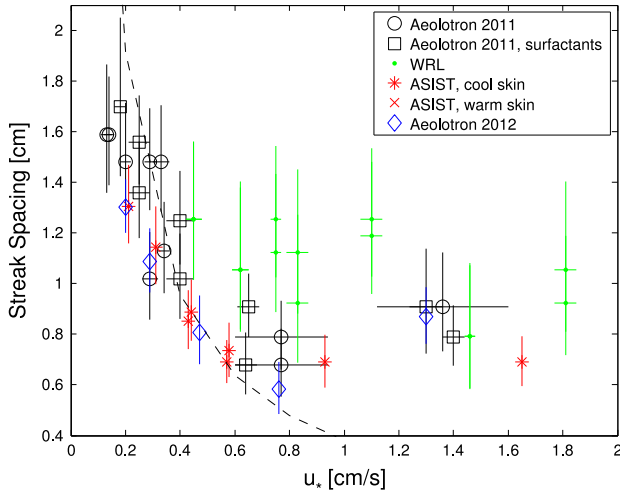
Figure 8. Streak spacing against u^* obtained from data measured at the Aeolotron, Heidelberg (IR camera: Thermosensorik CMT 256) without (black circles) and with surfactants (black squares), at the Aeolotron, Heidelberg (IR camera: IRCAM Velox 327k M) (blue diamonds), at WRL (green dots), Sydney, and at the ASIST facility in Miami (red stars). Y error bars mark 1σ intervals of the underlying log normal distribution and represent a measure of the variability of the system. A linear fit describes the distribution reasonably well up to a friction velocity of $\sim$0.7 cm/s. From then on the obtained streak spacings seem to be independent of u^*. The dotted line shows the trend for shear induced turbulence according to $lu^*/\nu = 100$.
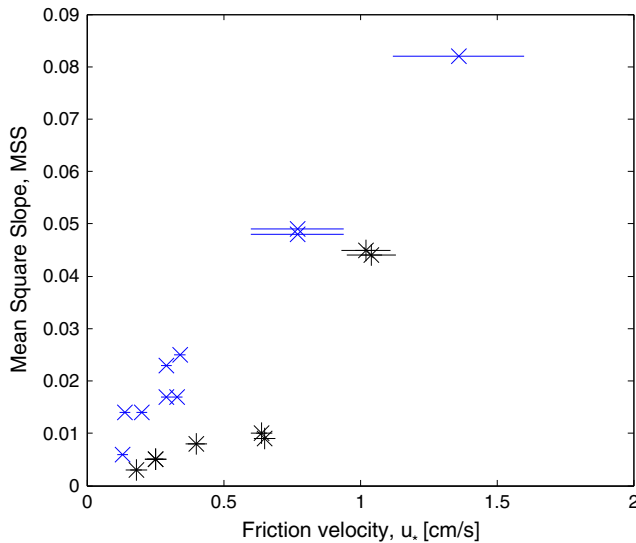

Figure 9. Development of Mean Square Slope (MSS) with increasing wind speeds. Measurements at the Aeolotron, Heidelberg. Blue crosses: clean surface; black crosses: surfactant (Triton X-100) suppresses capillary waves but not gravity waves.
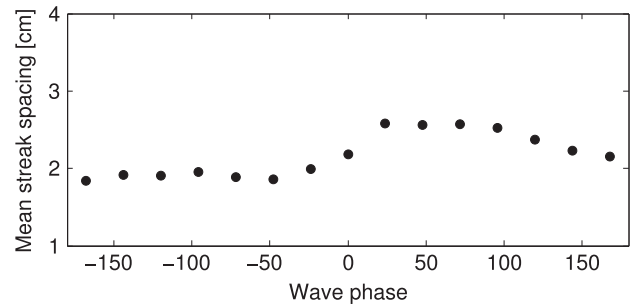

Figure 10. Mean spacing along the wave phase. Incipient breaking case, $u_* = 1.11$ cm/s.

Langmuir circulation thus the La^{-1} number measured here will presumably be larger than it was at the inception of LC.

5. Discussion and Conclusion

[92] Two turbulence generating mechanisms have been identified to play a role in the generation of the surface heat pattern. The small-scale structures termed fish scales result from wind stress only and are therefore considered as shear induced turbulence. The larger-scale cold surface streaks have been identified as Langmuir circulation induced as described by *Caulliez* [1998], *Melville et al.* [1998], and *Veron and Melville* [2001].

[93] The nature of this pattern changes with increasing wind stress and surface condition, although differently for shear-induced turbulence (1) and LC (2).

[94] 1. The small-scale heat pattern is substantially dependent on wind speed, indicating that shear stress only is the generating mechanism. The analysis of the streak spacing yields a log normal distribution. This is qualitatively consistent with the findings of *Tsai et al.* [2005] on numerical data and also to the work of *Smith and Metzler* [1983] and *Nakagawa and Nezu* [1981] on the spacing of low speed streaks near a no-slip wall thereby indicating the similarity of the causing process. In the regime of very low wind speeds streak spacing decreases linearly with wind speed and this behavior is the same as for low speed streaks near a no-slip wall. Surprisingly, above a friction velocity of $\sim$0.7 cm/s the streak spacing seems to become relatively independent of wind stress. Considering that tangential stress is the driving factor and that the fraction of tangential stress has been reported to remain constant as more of the wind stress is transformed to wave form drag [*Banner and Peirson*, 1998], this could be an explanation for the stagnating streak spacing. Although, the turbulence in the shear layer is highly non-isotropic, a scale can be calculated in analogy to the smallest possible eddy size for isotropic turbulence, the Kolmogorov scale. We estimate the energy dissipation rate $\langle \epsilon \rangle = u^3/l$, with u the velocity and l the integral length scale. Because of the anisotropy, we used the surface velocity in y direction as u and the largest observed streak spacings as l. The result of the rough estimation is a length scale η of order $\mathcal{O}(0.1$ cm). This would also lead to a minimum cell size of anisotropic turbulence. The influence of viscosity does not become apparent in our result and the rough estimation of changes of smallest possible eddy sizes shows that an increase in temperature by 10 K results in a
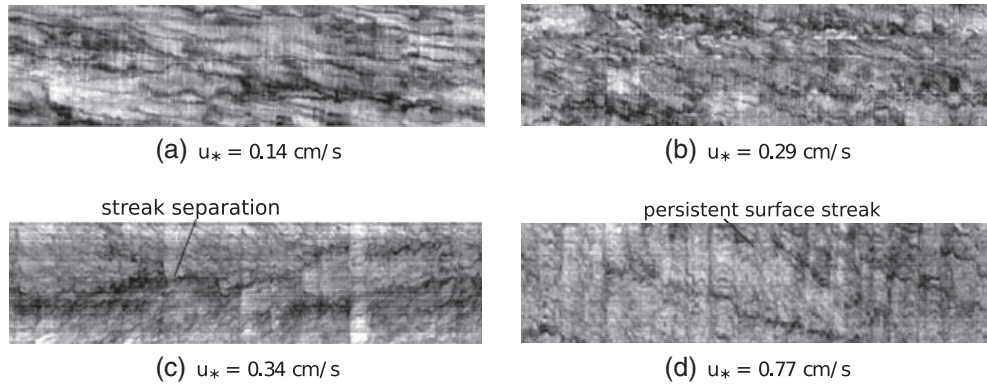
(a) $u_* = 0.14$ cm/s

(b) $u_* = 0.29$ cm/s

streak separation

persistent surface streak

(c) $u_* = 0.34$ cm/s

(d) $u_* = 0.77$ cm/s

Figure 11. Aeolotron, clean surface conditions, and temporal development of structures at the water surface. Shown in both Figures 11 and 12 is the temporal development of one line in a stack of infrared images. Each image shows a 20 s long sequence of the development at a set spatial position. (One line at fixed position in cross-wind direction was taken from each image of a sequence).
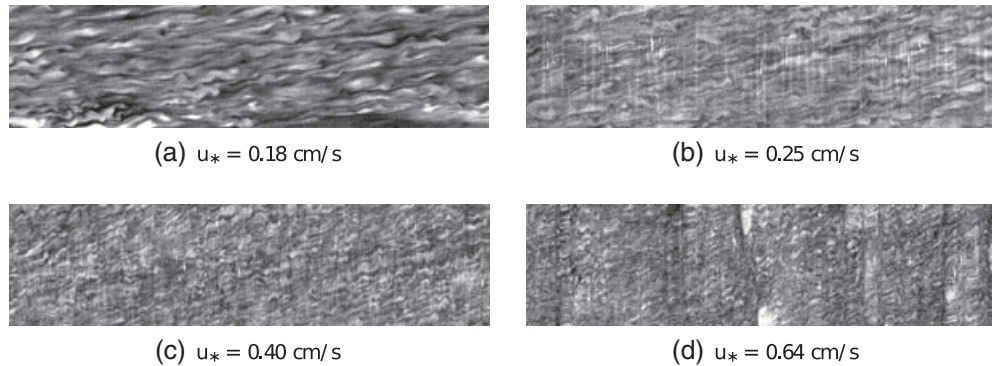

(a) $u_* = 0.18$ cm/s

(b) $u_* = 0.25$ cm/s

(c) $u_* = 0.40$ cm/s

(d) $u_* = 0.64$ cm/s

Figure 12. Aeolotron, Triton X-100, temporal development of structures at the water surface.

20% change of the microscales. As the variability of streak spacings is generally very high, this is difficult to determine.

[95] 2. Larger-scale cold streaks in comparison are not as dependent on wind stress but their appearance and spacing are determined by the surface wave field thereby showing they are indeed Langmuir circulation, as described in *Melville et al.* [1998], *Veron and Melville* [2001], and *Caulliez* [1998]. The analysis of the streak spacing in comparison to wave field parameters allows a comparison to the data presented by *Melville et al.* [1998] and *Veron and Melville* [2001] and the predictions of *Leibovich and Paolucci* [1981].

[96] Even though the conditions were different (measurements were conducted not just after the onset of waves but in a fully developed wave field), our measurements match those of *Melville et al.* [1998] very well for identical Langmuir numbers. Higher inverse Langmuir numbers lead to higher values of normalized Langmuir wave numbers and thereby follow the trend suggested of the neutral stability theory by *Leibovich and Paolucci* [1981].

[97] In recent work by *McKenna and McGillis* [2004] and *Veron et al.* [2011], it has been shown that surface divergence has an enormous effect on surface heat and gas fluxes.

[98] We conclude that the here presented method based on passive thermography and the subsequent analysis of streak spacing provide a valuable tool to assess features of near-surface turbulence and gain insight into turbulent processes that are a controlling mechanism in air-sea gas exchange.
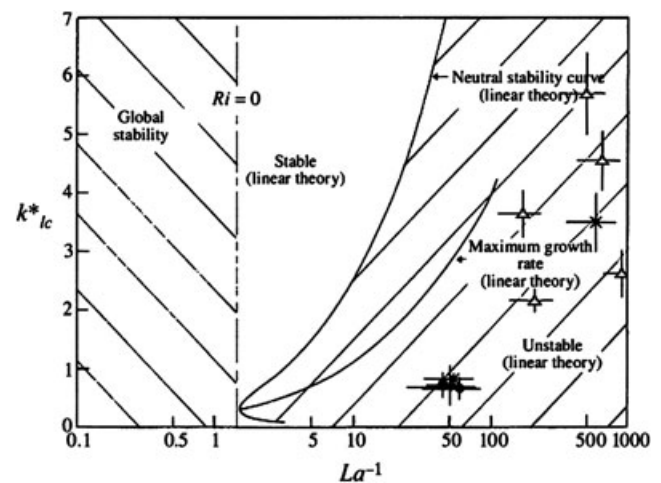

Figure 13. $k_{LC}^* = \frac{k_{LC}}{k_{wave}}$ against inverse Langmuir number La^{-1}. Neutral stability theory by *Leibovich and Paolucci* [1981] compared with the data obtained by *Melville et al.* [1998] and the data measured at WRL under the presence of mechanical waves (open triangles) and the data from Aeolotron (crosses).

References

Banner, M. L., and W. L. Peirson (1998), Tangential stress beneath wind-driven airwater interfaces, *J. Fluid Mech.*, *364*, 115–145.

Bopp, M. (2011), Messung der Schubspannungsgeschwindigkeit am Heidelberger Aeolotron mittels der Impulsbilanzmethode, Master's Thesis, University of Heidelberg.

Breimann, L. (2001), Random forests, *Mach. Learn.*, *45*, 5–32.

Caulliez, G. (1998), The generation of the first visible wind waves, *Phys. Fluid*, *10*(4), 757–759.

Chernyshenko, S. I., and M. F. Baig (2005), The mechanism of streak formation in near-wall turbulence, *J. Fluid Mech.*, *544*, 99–131, doi: doi:10.1017/S0022112005006506.

Chini, G. P. (2008), Strongly nonlinear Langmuir circulation and Rayleigh-Bénard convection, *J. Fluid Mech.*, *614*, 39–65, doi: 10.1017/S0022112008003133.

Craik, A. D. D., and S. Leibovich (1976), A rational model for Langmuir circulations, *J. Fluid Mech.*, *73*, 401–426.

Eisenhauer, D. (2011), Aufbau eines Messsystems zur Amplitudenmessung von Schwerewellen im Aeolotron, Master's thesis, University of Heidelberg.

Garbe, C. S., H. Haußecker, and B. Jähne (2002), Measuring the sea surface heat flux and probability distribution of surface renewal events, in *Gas Transfer at Water Surfaces*, edited by E. Saltzman, M. Donelan, W. Drennan, and R. Wanninkhof, Geophysical Monograph, vol. 127, pp. 109–114, American Geophysical Union, Washington D. C.

Garbe, C. S., U. Schimpf, and B. Jähne (2004), A surface renewal model to analyze infrared image sequences of the ocean surface for the study of air-sea heat and gas exchange, *J. Geophys. Res. C Oceans*, *109*(C8), 1–18, doi:10.1029/2003JC001802.

Gemmrich, J., and L. Hasse (1992), Small-scale surface streaming under natural conditions as effective in air-sea gas exchange, *Tellus B*, *44*, 150–159.

Grassl, H. (1976), The dependence of the measured cool skin of the ocean on wind stress and total heat flux, *Boundary-Layer Meteorology*, *10*, 465–474.

Handler, R. A., and G. B. Smith (2011), Statistics of the temperature and its derivatives at the surface of a wind-driven air-water interface, *J. Geophys. Res.*, *116*(C8), C06021, doi:10.1029/2010JC006496.

Handler, R. A., G. B. Smith, and R. I. Leighton (2001), The thermal structure of an air-water interface at low wind speeds, *Tellus*, *53*, 233–244.

Handler, R. A., I. Savelyev, and M. Lindsey (2012), Infrared imagery of streak formation in a breaking wave, *Phys. Fluids*, *24*, 1070–6631, doi: 10.1063/1.4769459.

Haußecker, H., S. Reinelt, and B. Jähne (1995), Heat as a proxy tracer for gas exchange measurements in the field: Principles and technical realization, in *Air–Water Gas Transfer: Selected Papers from the Third International Symposium on Air–Water Gas Transfer*, edited by B. Jähne, and E. C. Monahan, AEON Verlag & Studio, Hanau, Heidelberg, 405–413.

Haußecker, H., U. Schimpf, C. S. Garbe, and B. Jähne (2002), Physics from IR image sequences: Quantitative analysis of transport models and parameters of air-sea gas exchange, in *Gas Transfer at Water Surfaces*, edited by E. Saltzman, M. Donelan, W. Drennan, and R. Wanninkhof, Geophysical Monograph, vol. 127, pp. 103–108, American Geophysical Union, Washington, D. C.

Hunt, J., S. Belcher, D. Stretch, S. Sajjadi, and J. Clegg (2011), Turbulence and wave dynamics across gas-liquid interfaces, in *Gas Transfer at Water Surfaces 2010*, edited by S. Komori, W. McGillis, and R. Kurose, Kyoto University Press, Kyoto.

Jähne, B., and H. Haußecker (1998), Air-water gas exchange, *Annu. Rev. Fluid Mech.*, *30*, 443–468.

Jessup, A. T., et al. (1997), Infrared remote sensing of breaking waves, *Nature*, *385*, 52–55.

Leibovich, S. (1983), The form and dynamics of Langmuir circulations, *Annual Review Fluid Mechanics*, *15*, 391–427.

Leibovich, S., and S. Paolucci (1981), The instability of the ocean to Langmuir circulations, *J. Fluid Mech.*, *102*, 141–167.

McKenna, S. P., and W. R. McGillis (2004), The role of free-surface turbulence and surfactants in air-water gas transfer, *Int. J. Heat Mass. Tran.*, *47*, 539–553, doi:10.1016/j.ijheatmasstransfer.2003.06.001.

Melville, W. K., R. Shear, and F. Veron (1998), Laboratory measurements of the generation and evolution of Langmuir circulations, *J. Fluid Mech.*, *364*, 31–58.

Mizuno, M. (2011), Effects of the mechanical wave propagating in the wind direction on currents and stress across the air-water interface, in *Gas Transfer at Water Surfaces 2010*, edited by S. Komori, W. McGillis, and R. Kurose, pp. 104–118, Kyoto University Press, Tokyo.

Nakagawa, H., and I. Nezu (1981), Structure of space-time correlation of bursting phenomena in an open-channel flow, *J. Fluid Mech.*, *104*, 1–43.

Peirson, W. L. (1997), Measurement of surface velocities and shears at a wavy air-water interface using particle image velocimetry, *Exp. Fluids*, *23*, 427–437.

Rashidi, M., and S. Banerjee (1990), The effect of boundary conditions and shear rate on streak formation and breakdown in turbulent channel flows, *Phys. Fluids*, *2*, 1827–1838.

Rocholz, R., S. Wanner, U. Schimpf, and B. Jähne (2011), Combined visualization of wind waves and water surface temperature, in *Gas Transfer at Water Surfaces 2010*, edited by S. Komori, W. McGillis, and R. Kurose, pp. 496–506, Kyoto University Press, Tokyo.

Sanjou, M., I. Nezu, and Y. Akiya (2011), PIV measurements of Langmuir circulation generated by wind-induced water waves, in *Gas Transfer at Water Surfaces 2010*, edited by S. Komori, W. McGillis, and R. Kurose, pp. 129–137, Kyoto University Press, Tokyo.

Schimpf, U., C. Garbe, and B. Jähne (2004), Investigation of transport processes across the sea surface microlayer by infrared imagery, *J. Geophy. Res.*, *109*(C8), C08S13, doi:10.1029/2003JC001803.

Schimpf, U., H. Haußecker, and B. Jähne (1999), Thermography for small-scale air-sea interaction, in *Handbook of Computer Vision and Applications*, edited by B. Jähne, P. Geißler, and H. Haußecker, Systems and Applications, chapter 35, vol. 3, Academic Press, 751–762.

Scott, N. V., Handler, R.A., and G. B. Smith (2008), Wavelet analysis of the surface temperature field at an air-water interface subject to moderate wind stress, *Int. J. Heat Fluid Flow*, *29*, 1103–1112, doi: 10.1016/j.ijheatfluidflow.2007.11.002.

Smith, C. R., and S. Metzler (1983), The characteristics of low-speed streaks in the near-wall region of a turbulent boundary layer, *J. Fluid Mech.*, *129*, 27–54.

Smith, G. B., R. A. Handler, and N. Scott (2007), Observations of the structure of the surface temperature field at an air-water interface for stable and unstable cases, in *Transport at the Air Sea Interface—Measurements, Models and Parameterizations*, edited by C. S. Garbe, R. A. Handler, and B. Jähne, pp.205–222, Springer-Verlag, Heidelberg.

Soloviev, A., and P. Schlüssel (1994), Parameterization of the cool skin of the ocean and of the air-ocean gas transfer on the basis of modeling surface renewal, *J. Phys. Oceanogr.*, *24*, 1339–1346.

Soloviev, A., S. Matt, M. Gilman, H. Hühnerfuss, B. Haus, D. Jeong, I. Savelyev, and M. Donelan (2011), Modification of turbulence at the air-sea interface due to the presence of surfactants and implications for gas exchange. Part I: Laboratory experiment, in *Gas Transfer at Water Surfaces 2010*, edited by S. Komori, W. McGillis, and R. Kurose, pp. 285–298, Kyoto University Press, Tokyo.

Sommer, C., C. Straehle, U. Koethe, and F. A. Hamprecht (2011), Ilastik: Interactive learning and segmentation toolkit, in *8th IEEE International Symposium on Biomedical Imaging (ISBI 2011)*, Chicago.

Thorpe, S. A. (2004), Langmuir Circulation, *Annu. Rev. Fluid. Mech.*, *36*, 55–79, doi:10.1146/annurev.fluid.36.052203.071431.

Tsai, W.-T., S.-M. Chen, and C.-H. Moeng (2005), A numerical study on the evolution and structure of a stress-driven free-surface turbulent shear flow, *J. Fluid Mech.*, *545*, 163–192, doi:10.1017/S0022112005007044.

Veron, F., and K. Melville (2001), Experiments on the stability and transition of wind-driven water surfaces, *J. Fluid Mech.*, *446*, 25–65.

Veron, F., K. Melville, and L. Lenain (2011), The effects of small-scale turbulence on air-sea heat flux, *J. Phys. Oceanogr.*, *41*, 205–220, doi: 10.1175/2010JPO4491.1.

Wanninkhof, R., G.-H. Park, D. B. Chelton, and C. M. Risien (2011), Impact of small-scale variability on air-sea CO_2 fluxes, in *Gas Transfer at Water Surfaces 2010*, edited by S. Komori, W. McGillis, and R. Kurose, pp. 431–444, Kyoto University Press, Tokyo.

Zappa, C. J., W. E. Asher, and A. T. Jessup (2001), Microscale wave breaking and air-water gas transfer, *J. Geophys. Res. C Oceans*, *106*, 9385–9391.